Trabecular-like Ti-6Al-4V scaffolds for orthopedic: fabrication by selective laser melting and in vitro biocompatibility

Article (Accepted Version)

Accepted Manuscript

Title: Trabecular-like Ti-6Al-4V scaffolds for orthopedic: fabrication by selective laser melting and *in vitro* biocompatibility

Authors: Huixin Liang, Youwen Yang, Deqiao Xie, Lan Li, Ning Mao, Changjiang Wang, Zongjun Tian, Qing Jiang, Lida Shen

PII: S1005-0302(19)30023-4
DOI: https://doi.org/10.1016/j.jmst.2019.01.012
Reference: JMST 1463

To appear in:

Received date: 19 November 2018
Revised date: 17 December 2018
Accepted date: 14 January 2019

Please cite this article as: Liang H, Yang Y, Xie D, Li L, Mao N, Wang C, Tian Z, Jiang Q, Shen L, Trabecular-like Ti-6Al-4V scaffolds for orthopedic: fabrication by selective laser melting and *in vitro* biocompatibility, *Journal of Materials Science and amp; Technology* (2019), https://doi.org/10.1016/j.jmst.2019.01.012

Trabecular-like Ti-6Al-4V scaffolds for orthopedic: fabrication by selective laser melting and *in vitro* biocompatibility

Huixin Liang [1,†], Youwen Yang [2,3,†], Deqiao Xie [1], Lan Li [4], Ning Mao [1,6], Changjiang Wang [5], Zongjun Tian [1], Qing Jiang [4,*], Lida Shen [1,*]

[1] *College of Mechanical and Electrical Engineering, Nanjing University of Aeronautics and Astronautics, Nanjing 210016, China*

[2] *State Key Laboratory of High Performance Complex Manufacturing, Central South University, Changsha 410083, China*

[3] *Jiangxi University of Science and Technology, Ganzhou 341000, China*

[4] *Department of Sports Medicine and Adult Reconstructive Surgery, Nanjing University Medical School Affiliated Drum Tower Hospital, Nanjing 210008, China*

[5] *Department of Engineering and Design, University of Sussex, Sussex House, Brighton BN19RH, United Kingdom*

[6] *Suzhou Kangli Orthopedics Instrument Co. Ltd., Suzhou 215624, China*

†These authors contributed equally.

*Corresponding authors.

E-mail addresses: ldshen@nuaa.edu.cn (Lida Shen); qingj@nju.edu.cn (Qing Jiang).

[Received 19 November 2018; Received in revised form 17 December 2018; Accepted 14 January 2019]

Porous metal scaffolds play an important role in the orthopedic field, due to their wide applications in prostheses implantation. Some previous studies showed that the scaffolds with trabecular bone structure reconstructed via computed tomography had satisfactory biocompatibility. However, the reverse modeling scaffolds were inflexible for customized design. Therefore, a top-down designing biomimetic bone scaffold with favorable mechanical performances and cytocompatibility is urgently demanded for orthopedic implants. An emerging additive manufacturing technique, selective laser melting, was employed to fabricate the trabecular-like porous Ti-6Al-4V scaffolds with

varying irregularities (0.05-0.5) and porosities (48.83%-74.28%) designed through a novel Voronoi-Tessellation based method. Micro-computed tomography and scanning electron microscopy were used to characterize the scaffolds' morphology. Quasi-static compression tests were performed to evaluate the scaffolds' mechanical properties. The MG63 cells culture *in vitro* experiments, including adhesion, proliferation, and differentiation, were conducted to study the cytocompatibility of scaffolds. Compressive tests of scaffolds revealed an apparent elastic modulus range of 1.93-5.24 GPa and an ultimate strength ranging within 44.9-237.5 MPa, which were influenced by irregularity and porosity, and improved by heat treatment. Furthermore, the *in vitro* assay suggested that the original surface of the SLM-fabricated scaffolds was favorable for osteoblasts adhesion and migration because of micro scale pores and ravines. The trabecular-like porous scaffolds with full irregularity and higher porosity exhibited enhanced cells proliferation and osteoblast differentiation at earlier time, due to their preferable combination of small and large pores with various shapes. This study suggested that selective laser melting-derived Ti-6Al-4V scaffold with the trabecular-like porous structure designed through Voronoi-Tessellation method, favorable mechanical performance, and good cytocompatibility was a potential biomaterial for orthopedic implants.

Keywords: Irregular porous structure; Selective laser melting; Voronoi-Tessellation; Mechanical performance; *In vitro* study

1. Introduction

Porous metal scaffolds (PMS) play an important role in the orthopedic field, due to their wide applications in prostheses implantation, such as artificial joint replacement and repair of bone defects caused by infection, trauma, or tumor resection[1]. Specifically, on one hand, its porous structure could mitigate risks associated with stress shielding and form a strong bone-implant interface by achieving a closer mechanical property match of bone, while providing an appropriate medium for nutrient transport, bone cell ingrowth and differentiation[2-4]. On the other hand, in contrast to ceramics and polymers[5, 6], metal materials have the advantages of balanced mechanical properties and unique scaffold structures, making them widely applicable to orthopedic implants[7-10]. Among them, titanium and its alloys are biologically preferable and corrosion

resistant because of a naturally occurring passive oxide layer on the surface, while still maintaining strong mechanical properties, low modulus of elasticity, and a high strength to weight ratio[11, 12].

In general, bone scaffolds has either regular or irregular porous structures. Regular porous structures are usually constructed by a simple repletion of the unit cell or the triply periodic minimal surface, etc.[13, 14]. The uniform pore size, consistent unit morphology, and controllable porosity influence the mechanical behavior and the biocompatibility of regular porous scaffolds[15-17]. However, the human trabecular bone does not have the same pore size and profile, or the immutable local porosity. The homogeneity of regular porous scaffolds might not obtain a satisfactory cellular response *in vitro* and *in vivo*. In contrast, the irregular porous structures present random variations in pore's geometry and dimension. The resulting range of pore size distribution, changeable pore profiles and different local porosities could be the extra potential factors that improve the biocompatibility of porous scaffolds in bone tissue engineering (BTE). Some related research results had proved that the irregular porous structures analogous to cancellous were more conducive to cells growth, which shown the superiority of irregular porous structure[18, 19].

A majority of the irregular porous scaffolds are constructed through the image based reverse modeling method, the mathematical modeling method, or their combination in order to imitate natural bone characteristics at all levels (i.e. mechanical, biological, mass transport and microstructure geometry)[20-22]. Noteworthy, the Voronoi-Tessellation based mathematical modeling method presents excellent performances in constructing approximate models of natural irregular porous materials, like collagen networks[23], foams[24], and biological cells structures[25, 26]. Unsurprisingly, this nature-inspired geometric representation method has received much attention in its ability to construct biomimetic porous scaffolds for BTE because of the inherent bionics characteristic. Fantini et al.[27] constructed the biomimetic full-interconnected porous scaffolds with the trabecular-like structure and customized geometry based on the Voronoi-Tessellation method. S. Gómez et al.[28] extracted the seeds from the micro-CT images of the trabecular bone, and modeled the trabecular structure more precisely with the Voronoi-Tessellation principle, exactly matching the main histomorphometric indices of the trabecular bone, which could require additional computational resources and efforts. However, no related studies regarding the mechanical performance and biocompatibility of Ti-based trabecular-like scaffolds based on Voronoi-Tessellation have been reported.

The additive manufacturing (AM) techniques have been described as crucial production

techniques towards a more controlled bone scaffolds due to their impressive capability of producing porous structures with a controlled architecture precisely owing to their layer-wise building approach and their direct link with a computer-aided design (CAD) model[29]. As one of recently developed AM techniques, selective laser melting (SLM) process creates functional and complex metal parts directly, bringing a high degree of freedom to design[30]. Compared to the conventional manufacturing techniques, the SLM offers a wide range of advantages, including reduction of production steps, a high level of flexibility, a high material use efficiency, and a near net shape production[31]. Moreover, the SLM process is capable of producing complex geometrical features that cannot be obtained using conventional production routes due to the additive and layer-wise production. The SLM-built porous biological metal scaffolds that have presented positive results in both *in vitro* and *in vivo* studies[32].

On the basis of previous studies, we proposed a new and convenient method of modeling irregular scaffold to mimic the trabecular structure based on Voronoi-Tessellation, which separated bounding box volume into several small areas according to desired pattern (isotropic, gradient, and topological) and randomly generated seeds in the respective area, resulting in the high level of controllability in parameters successfully [33]. In this work, in order to systematically investigate the performances in BTE of the scaffolds based on the proposed method, the porous samples with varying irregularity and porosity were designed and fabricated by the SLM process with Ti-6Al-4V powders. In details, The manufacturability and morphology features of the scaffolds fabricated through SLM were evaluated. The effects of irregularity, porosity and heat treatment on the mechanical properties of as-built porous scaffolds were discussed. Significantly, cellular response to scaffolds with varying irregularities and porosities was also studied by culturing the MG63 cells *in vitro*.

2. Material and methods

2.1. Materials

The commercial Ti-6Al-4V extra low interstitial (ELI) powder supplied by EOS GmbH was used in the experiment, meeting ISO 5832-3 and ASTM F1472. As an optimized medical material, the trace elements of Ti-6Al-4V ELI such as O, N, H, C, and Fe were relatively low in content (Table 1). As shown in the scanning electron microscopy (SEM) image of Fig. 1 (ΣIGMA, Zeiss,

German), the powder had high sphericity and few satellite spheres with a particle size range of 15-53 μm.

2.2. Design and fabrication of irregular porous scaffolds

A probability sphere method based on Voronoi-Tessellation was used to generate the random seeds in order to construct irregular porous structures with full connectivity (Fig. 2(a))[33]. The porous scaffolds with different porosities and irregularities could be modeled using computer aided design (CAD) software Rhinoceros with a Grasshopper plugin (version 0.9.0076) and Boolean operations. The porosity and irregularity of scaffolds were determined through adjusting seeds number and scale coefficient of K. It is important to note that the corresponding scaffold will become a type of hexagonal lattice structure with paired cylinder-shaped struts when the irregularity reaching zero.

The specimens were fabricated using an SLM machine (EOSINT M290; EOS GmbH, Germany) with optimized processing parameters (Table 2). Selective laser melting of porous scaffolds was characterized by a controllable and precise layer-wise material addition process that allowed generation of complex structures by selectively melting successive layers of metal powder, using a focused and computer controlled laser beam (Fig. 2(b))[34].

Two sets of cylindrical specimens were fabricated with a diameter of 12 mm and two heights of 16 mm and 3 mm for various tests (Fig. 2(c)). Set 1 of specimens had irregularities (ε) of 0.06, 0.25, and 0.5 with the same designed porosity (Φ) of 70%±1% under seeds number of 2000 and scale coefficient (K) of 0.65, having the approximately same surface area and strut size. Set 2 of specimens had designed porosities (Φ) of 55%±1%, 68%±1% and 80%±1% and the same irregularity (ε) of 0.5 under seeds number of 1200 and scale coefficients (K) of 0.55, 0.65, 0.75, having the gradually decreasing surface area and strut size. The specimens (Ø 12 mm × 3 mm) for cell culture were cut off from the base plate via wire electrical discharge machining (WEDM).

2.3. Measurement and characterization

A micro-computed tomography (μCT) scanner (FF35 CT; YXLON International, Germany) with a 17 μm resolution was used to scan the samples (Ø 12 mm × 3 mm) at 200 kV and 50 μA. The samples were rotated over 360° in steps of 0.36° during the acquisition. Two-dimensional (2D)

projection images (n=1000) were collected. The 3D models of the fabricated samples were reconstructed through these slice images data using commercially available software (VGStudio MAX 3.0; Volume Graphics GmbH, Germany). Based on the direct observation from cross-section method[35], the pore size distribution of the as-built porous scaffolds was characterized through the freeware (ImageJ 1.51; National Institutes of Health, USA) to analyze the section's μCT images with thresholding processing obtained from the same position of the reconstructed 3D models. The surface micro-topography of struts of SLM-produced porous scaffolds was observed by a field-emission scanning electron microscopy (S-4800; Hitachi, Ltd., Japan). And the porosity (Φ) of the fabricated scaffold was obtained as follows:

$$\Phi = 1 - \frac{V_s}{V_C} \qquad (1)$$

where V_s is the volumes of the SLM-produced scaffolds measured from reconstructed 3D models by using the commercially available software (Magics 21.0.0; Materialise, Belgium) and V_C is the total volume of the solid cylinder that has the same outline size with scaffold.

2.4. Heat treatment and Mechanical testing

According to GJB 3763A-2004 standard, two heat treatment processes for the mechanical test samples were executed in a vertical tube furnace in an argon atmosphere with a heating rate of approximately 5 °C/min: stress relief annealing at 600 °C for 60 min and furnace cooling (FC); full annealing at 840 °C for 30 min and furnace cooling.

The static compression tests were performed using an electronic universal testing machine (CMT5105; MTS System Corporation, America) with a 100 kN load cell. According to the ISO 13314:2011 standard for the compression of porous and cellular metals, the pressure head speed was calculated to obtain an initial compression strain rate between 10^{-3} s^{-1} and 10^{-2} s^{-1}. This corresponded to 2.5 mm/min for the samples with a height of 16 mm. As described in ISO 13314 (Fig. 3), the plateau stress (σ_{pl}) was determined as the arithmetical mean of the stresses with a 20% to 40% compressive strain. Known as apparent elastic modulus of porous and cellular metals, the elastic modulus was the slope of the elastic straight lines determined by elastic loading between 70% and 20% of plateau stress (σ_{pl}). The ultimate strength was defined by first maximum compressive strength, which determined the load-bearing capacity of the porous scaffolds. These were extracted

from the stress-strain curve and recorded for each sample (n=3).

2.5. Finite element analysis of as-designed models

To compare the predicted and tested mechanical properties of the as-built samples, the finite element analysis (FEA) on ideal as-designed porous structures were performed using the commercial software (ABAQUS 2016; Dassault Systemes Simulia Corp., USA) with the elastic modulus of 105 GPa, Poisson's ratio of 0.3, and the yield strength of 830 MPa. The FEA model was assumed to be linear, elastic, and homogeneous. The loading conditions and the boundary constraints were set based on a previous study[36]. The top of cylindrical specimen was loaded with a pressure of 80 MPa while the bottom boundary was fixed. The deformation and the stress distribution under pressure were investigated through parameter settings, model meshing and solving.

2.6. Cell culture

The as-built Ti-6Al-4V scaffolds were cleaned and modified prior to cell culture experiment. The specimens were washed ultrasonically in 95% ethanol and distilled water for 30 min each. Next, the specimens were first soaked in a 5 mol/L NaOH solution at 60 °C for 24 h. Lastly, the specimens were further washed ultrasonically in distilled water for 10 min and then dried for at least 24 h in order to stabilize the oxide layer before cells culture before being sterilized..

An *in vitro* cells culture was carried out using MG63 cells. The scaffolds were pre-wetted with cell culture medium, which consisted of Dulbecco's modified eagle medium (DMEM), 10% fetal bovine serum (FBS, Gibco), and 1% antibiotics/a for 2 h and then air-dried in sterile conditions. For each scaffold, 20,000 MG63 cells (in 60 µl cell suspension) were drop seeded and statically incubated for 4 h at 37 °C to facilitate cell attachment. The DMEM supplemented with 10% fetal bovine serum, 100 U/mL penicillin and 100 mg/mL streptomycin were used as culture medium. The cell-seeded scaffolds were transferred to a 24-well plate and cultured in culture medium after 4 h, which was refreshed every 2 d.

Fluorescent staining was used to study the cell viability. After being cultured for 1 day, MG63 cells were digested from the scaffolds and washed with the phosphate buffer saline (PBS, Grand Island Biological Co., USA). Then cells were treated with 5 µmol/L calcein-AM and 4 µmol/L

ethidium homodimer-1 (LIVE/DEAD, Life Technologies, California, USA) in Dulbecco's phosphate buffered saline for 20 min at 37 °C. The stained cells were gently rinsed twice with PBS and then mounted onto glass slides for fluorescence microscopy observation (BX60, Olympus, Japan) (n_1=1). SEM observation was used to study the cell adhesion on the scaffolds. After being cultured for 3 d, the cell-seeded scaffolds were rinsed with PBS, and then soaked in 2.5% glutaraldehyde solution (Shanghai Likang Disinfectant Hi-tech Co., Ltd, China) for 2 h to fix the adhered cells. Afterwards, the scaffolds were dehydrated in a gradient ethanol/distilled water mixture (50%, 60%, 70%, 80%, 90%, and 100%) for 10 min each and dried in a hexamethyldisilazane (HMDS, Aladdin Industrial Corporation, China). The adhered cells on the scaffolds were observed under SEM. CCK-8 assay was used to investigate the cells proliferation. After being cultured for 1, 3 and 5 d, the adhered MG63 cells were digested from the scaffolds and incubated with 10 μL CCK-8 (5 mg/mL, Sigma-Aldrich, St. Louis, MO, USA) for 2 h in 37 °C, then the absorbance was measured at 450 nm by paradigm detection platform (BECK MAN, S. Kraemer Boulevard Brea, CA) (n=3). The alkaline phosphatase (ALP) activity was measured to evaluate the osteogenic differentiation of the cells. After being cultured for 14 d, the cells on the scaffolds were washed twice with PBS and lysed in 0.1% Triton X-100. The ALP levels was measured using an Alkaline Phosphatase Assay Kit (Beyotime, China) at 405 nm (n=3).

3. Results

3.1. Morphological characterization

SEM was used to characterize the struts' surface topography and the local features of the as-built scaffolds (Fig. 4). Compared to as-designed model (Fig. 4(b)), the interconnected network architecture was accurately duplicated by the final scaffolds fabricated via SLM (Fig. 4(a)). It was observed that there were a large quantities of spherical particles on the surface of struts, including incomplete metal particles and welding particles (Fig. 4(d)), which were attached to the structure and should not result in detachment risk. The bonded particles had a similar particle size and morphology to the raw Ti-6Al-4V particles prior to melting, which formed pores and ravines (Fig. 4(c) and (d)), resulting in a rough surface morphology for porous scaffold struts.

As the main morphological parameters of a porous scaffold, the strut thickness, volume, surface area, porosity, and specific surface area of two sets of as-built specimens were measured,

calculated from the micro-CT data and compared to their respective design values (Table 3). Set 1 of the as-built scaffolds with irregularities (ε) of 0.06, 0.25, 0.5 had experimental porosities of 61.49% (D=-9.43), 62.65% (D=-7.36), and 63.95% (D=-5.55) and specific surface areas of 7.01 mm^{-1} (D=-3.4), 7.56 mm^{-1} (D=-2.5), and 8.4 mm^{-1} (D=-1.97), which were lower than the corresponding designed models. In details, the strut thicknesses of the as-built scaffolds were higher than the respectively designed values, resulting in the increased volumes and decreased surface area. It should be emphasized that the scaffold with the irregularity of 0.06 had the largest relative errors for porosity, specific surface area, and strut thickness between as-designed and as-manufactured values, while the scaffold with irregularity of 0.5 had the smallest. Similarly, set 2 of the as-built scaffolds with designed porosities of 55%±1%, 68%±1%, 80%±1% and the same irregularity (ε) of 0.5 also had lower experimental porosities of 48.83% (D=-5.9), 63.51% (D=-4.16), and 74.28% (D=-5.32) and specific surface areas of 5.03 mm^{-1} (D=-0.9), 6.28 mm^{-1} (D=-1.18), and 7.23 mm^{-1} (D=-2.58) than designs.

Quantitatively, the pore size was defined by the equivalent circle diameter of the irregular 2D pore. The pore size distributions of the porous scaffolds with different irregularities were depicted in Fig. 5, where hundreds of pores were measured and counted using the cross-section direct observation method based on the thresholding processing μCT images. The porous scaffold with a low irregularity of 0.06 had about 90% of pore sizes distributed in a range of 600-1000 μm intensively and only 10% of pore sizes smaller than 300 μm. Besides, most pores had relatively uniform contours with low curvatures (Fig. 5(a)). As the irregularity increased, the pore size distribution became wider and more homogeneous. In addition, the maximum pore size became bigger and the shape of pore became irregular. The porous scaffold with a higher irregularity of 0.25 had the pore sizes with multi-peak distribution, and the shapes of pores presented chaotic characteristic (Fig. 5(b)). As the irregularity level reached 0.5, the pore sizes followed the approximately normal distribution, where more than 50% of pores were in range of 400-1000 μm (Fig. 5(c)). Furthermore, most pores had diversified shapes and high curvature in 2D view.

3.2. Mechanical characterization

The results of the static compression tests of the as-built scaffolds with two different heat treatment processes were summarized in Fig. 6, including the representative stress-strain curves, the calculated elastic modulus, and the ultimate strengths based raw data. The stress-strain curves were

typical for porous biomaterials including the linear increase in stress with strain and a plateau region with fluctuating stresses (Fig. 6(a) and (b)). Besides, it was observed that the curves had an initial approximate parabola going upwards at the beginning of loading. This might be attributed to the uneven interface of contact between pressure head and porous samples or existed slight distortion of the struts[37-39].

Elastic modulus and ultimate strength are the pivotal characterization parameters for evaluating the mechanical performance of porous biomaterials. As shown in Fig. 6(c) and (e), the samples that have a designed porosity of 70%±1% and different irregularities, had an elastic modulus range of 3.22-3.92 GPa before heat treatment, which decreased gradually with the increase of irregularity. Meanwhile, the ultimate strength reached a value of 105.8-158 MPa, but did not have the same variation tendency with elastic modulus. In details, the original porous scaffold with the irregularity of 0.06 had the highest elastic modulus of 3.92 GPa and the corresponding highest ultimate strength of 158 MPa. And the porous scaffold with the irregularity of 0.25 had the lower elastic modulus of 3.57 GPa and the corresponding lowest ultimate strength of 105.8 MPa. However, the porous scaffold with the irregularity of 0.5 owned the lowest elastic modulus of 3.22 GPa and a higher ultimate strength of 123 MPa.

As illustrated in Fig. 6(d) and (f), without any heat treatments, the samples with an irregularity of 0.5 and various porosities possessed an elastic modulus range of 1.93-5.24 GPa and attendant large-scale ultimate strength range of 44.9-237.5 MPa. Moreover they all decreased as the porosity increased. In other words, the porous structures with higher porosity could obtain lower modulus and strength, which was in agreement with numerous previous studies about lattice structure, including seminal work of Gibson and Ashby[40]. With the application of Gibson-Ashby model, the elastic modulus (E) and ultimate strength (σ) of the original porous structure with different porosities were fitted as follows:

$$\sigma = 1112.05(1-\frac{\Phi}{100})^{2.25} \qquad (2)$$

$$E = 13.65(1-\frac{\Phi}{100})^{1.4} \qquad (3)$$

Notably, both two executed heat treatments had distinct impact on mechanical properties of as-built porous samples. More specifically, as indicated in Fig. 6(c)-(f), the elastic modulus and ultimate strength of samples all decreased by 5%-10% after full annealing (840 °C+FC). And it was evident that the curves of full annealing samples showed better yield ductility than others (Fig. 6(a)

and (f)). The stress relief annealing (600 °C+FC) did not show an obvious effect on the elastic modulus, however, it improved the porous samples' ultimate strength at a certain degree of less than 10%.

3.3. In vitro cell behavior

The executed live/dead staining after 1 d of *in vitro* culture showed that the cells on all the Ti-6Al-4V scaffolds had high viability (Fig. 7(a) and (b)). Most of the cells began to spread out, showing a typical fusiform appearance. More cells were observed in the scaffolds with an irregularity of 0.5. And the scaffolds with low porosity of 48.83% were effectively seeded with the most cells. In addition, based on the optical density (OD) values indicated in Fig. 7(c) and (d), it could be inferred that the cell numbers increased with a longer culture time in all groups, indicating their good cytocompatibility. The statistical analysis showed that all set 1 of samples had no significant difference in cell density for day 5. However, the scaffolds with irregularity of 0.5 had a significant higher cell density than the others for day 1 and day 3 (Fig. 7(c)). For the set 2 of samples, after 1 d culture, the cell density of scaffolds with a low porosity of 48.83% was relatively higher than the others. Significantly, as the culture time increased, the cell density of scaffolds with porosities of 63.51% and 74.28% were obviously higher than the other samples for day 5 (Fig. 7(d)).

Representative adhesion morphologies of MG63 cells cultivated on the scaffolds for day 3 showed that cells could adhere to the original surface of SLM-produced scaffolds well (Fig. 8). Cell migration ability was not visibly influenced by the structure irregularity and porosity in the early period of time. Moreover, the apparent cell migration behaviors of bridging the micro scale pores and ravines on the struts surface or smaller pores of scaffolds were captured by SEM.

After 14 d of *in vitro* culture, the ALP for all groups was detected (Fig. 9). A marked difference in ALP activity was found in scaffolds with different irregularities and porosities. Specifically, the ALP activity of scaffolds with relatively high irregularities of 0.5 was higher than the scaffolds with a relatively low irregularity of 0.05 in set 1. And the scaffolds with relatively high porosities of 63.51% and 74.28% had higher ALP activity than others in set 2. However, no significant difference between scaffolds with irregularities of 0.25 and 0.5 was observed, nor between the scaffolds with porosities of 63.51% and 74.28%.

4. Discussion

4.1. Design and selective laser melting irregular porous scaffolds

The growing demand for tailored and biomimetic scaffolds in bone tissue engineering poses a huge challenge to design and manufacturing of porous structures, which must take both geometric features and mechanical performances into consideration to obtain satisfactory biocompatibility. From the point of design, the reverse modeling based on the CT data could be an effective method for constructing the trabecular-like porous scaffold, but would be inefficient, inflexible and out of control in other aspects except morphology. Alternatively, the method of combining the controlled random seeds and Voronoi-Tessellation principle is a promising way to approximately imitate the trabecular structure. From the other point of manufacturing, it is difficult to control the internal pore geometry, pore size, and distribution for using the conventional fabrication techniques for designed porous models[41]. Facing this problem, SLM shows the superiority of high controllability and accuracy in fabricating complex metal parts, like porous Ti-based scaffolds[38].

The Voronoi-Tessellation based approach could effectively imitate the architecture of the healthy spongy bone with accurate full-interconnected trabecular-like structure by using the seeds stochastically distributed in the design volume (Fig. 10). In most cases, the seeds number and scale factor were discussed as the key parameters which can control the porosity, pore size, strut thickness, and cross section profile, etc. However, the irregularity of this kind of porous structure was rarely raised in any explicit manner, which could be the kernel issue when biomimetically imitating bone structure. In this work, the samples with heterogeneity in geometry and homogeneity in porosity were designed to have porosities of 50-80% accommodating natural trabecular bone (Fig. 10(a) and (b))[19], and accompanying variable strut thickness, etc. (Table 3). Moreover, it was emphasized that the randomness degree of seeds distribution could affect pore geometrical characteristic seriously, like pore size distribution and pore profile (Fig. 12), which was regarded as the irregularity of the porous structure based on Voronoi-Tessellation. The random seeds provided geometrical heterogeneity thus resulting in a really biomimetic shape. So the structure with full irregularity of 0.5 was most analogous to trabecular structure. Besides, for using the proposed method to imitate trabecular structure with varying porosity with location, the porous structure with gradient in porosity could be modeled through partitioning seeds' respective areas according gradient pattern (Fig. 10(c) and (d)).

The AM process of selective laser melting was competent in the production of porous scaffolds directly from metallic powders. However, this also brings some inherent discrepancies with respect to designed model. Similar results were observed in the previous works of Van et al.[16], Warnke et al.[32], Hollander et al.[42], Fantini et al.[43], Sing et al.[44], but not discussed systemically. Firstly, the SLM-produced scaffolds have very rough surface with pores and ravines, resulting from the adhesion of partly melted particles on the struts, which is universal phenomenon in SLM process. The presence of these particles on the struts could be due to two main following reasons (Fig. 11). On one hand, the raw particles on the boundary of hatching laser track laser path for the solid struts partially melt due to heat transfer from the melt pool to the surrounding powder bed[44]. On the other hand, the melt pool swallows particles proactively from surrounding powder layer through surface tension and violent convection movement, and solidified rapidly. Secondly, the SLM process makes a slight mismatch between as-designed and as-produced porous structures in geometrical size of struts. This is mainly due to the low thermal capacity of struts with smaller size (micron level). Specifically, when the consecutive laser beams overlap and melt the powder to form a tiny feature, the heat is more easily transferred by thermal conduction into the surrounding powder because of small thermal capacity of the solidified part. In this case, the molten pool tends to enlarge, thus absorbing more particles, making the size of SLM-produced struts exceed the designed values. Under the effect of these two points, the pore size decreased, the volume increased, and too small features were not created. As shown in Fig. 12, it was obvious that the as-built scaffolds had thicker struts, more rounded pore contour. Moreover, relatively small slender pores and sharp corners were missing, reducing the surface area. And the specific structure characteristic might affect the surface area deviations level. For example, the scaffold with an irregularity of 0.05 had more small slender pores than the others (Fig. 12(a) and (c)), therefore obtaining greater deviation (Table 3). It needs to say that this size deviation may can be neutralize from the design side.

4.2. Mechanical properties

The correlation between the mechanical properties and the geometrical parameters is crucial indicator to evaluate the controllability of porous structure, also primary basis for guiding design. In fact, the mechanical properties of irregular porous structure were closely related with its porosity and irregularity[45]. In addition, heat treatment also can affect mechanical performance of SLM-built samples.

As reported in Ref. [46-48], the human cancellous bone has a Young's modulus range of 0.1-4.5 GPa and ultimate strength range of 1.5-38 MPa. The cortical bone has a Young's modulus range of 5-23 GPa and ultimate strength range of 35-283 MPa. In this study, the mechanical behavior of the developed porous scaffolds in terms of their quasi-static mechanical properties was studied. The as-built Ti-6Al-4V scaffolds with porosities of 48.83%-74.28% presented a satisfying mechanical performance, an apparent elastic modulus range of 1.93-5.24 GPa and ultimate strength range of 44.9-237.5 MPa, which was in the same stiffness level as the cancellous bone but had more excellent stress resistance ability similar to cortical bone. Compared to the gradient regular porous structure[49-51], though they both consisted of pores with varied size, the gradient regular porous structure had obvious gradient phenomenon in mechanical behavior. And the irregular porous structure studied in this work presented a mechanical behavior like homogeneous porous structure with more reasonable match in modulus and strength. As a result, it is foreseeable that stress shielding is less likely to occur. Meanwhile the relatively high mechanical strength of the scaffolds provides enough mechanical support and prevents the structure's failure under mechanical loading.

Explicit correlations between the mechanical behavior and the porosity and irregularity were found based the results of mechanical experiments presented in Fig. 6. On one hand, the experimental apparent elastic modulus and ultimate strength decreased as the porosity increased, which were in accordance with the Gibson-Ashby model and has been corroborated by both synthetic constructs and human bone[40, 52, 53]. This experimental variation trend about porosity was also consistent with the simulation results obtained in this study. As depicted in Fig. 13(b), the structures with porosities of 54.73%, 67.67%, and 79.6% had maximum von Mises stress values of 1698 MPa, 3022 MPa, and 7805 MPa, respectively. Under the equivalent load pressure of 80 MPa, few struts of structure with porosity of 54.73% reached the yield strength of 830 MPa, but structure with porosity of 79.6% had the most struts undergoing yield deformation. The reason for this results is that the struts of the open porous structure mainly bear bending load during quasi-static compression[40]. And the porosity of porous structure is usually increased through lengthening or thinning the struts, resulting in weakening of resistance to bending. Therefore it is easy to understand that the structure with higher porosity has poorer compressive behavior. On the other hand, taking irregularity into consideration, the SLM-produced structures based on the proposed Voronoi-Tessellation based method exhibited a peculiar mechanical behavior under the same porosity level. This is because the unit cells of porous structure will gradually transform from

hexagonal structure with paired cylinder-shaped struts to irregular polyhedron structure with single struts during the increase in irregularity (Fig. 12), bringing the decrease in apparent elastic modulus. Some cell units' aberrations might have taken place, resulting in a sharp change in size of partial struts of structure with relatively low irregularity, which should get salient stress under compressive load. When irregularity reached the full-irregular level, a new stress balancing was founded in the high entropy environment of the structure, meliorating compressive strength. Just as predicted in Fig. 13(a), the structures with irregularities of 0.06, 0.25, and 0.5 had maximum von Mises stress values of 2707 MPa, 4153 MPa, and 3394 MPa respectively, revealing that the structure with irregularity of 0.25 had the most serious stress concentration.

Because of the rapid solidification of laser melting, the formation of high residual stress and out-of-equilibrium microstructure in the SLM-produced component are inevitable, which could result in undesirable effects including the promotion of cracking, the fatigue-failure and the part distortion[54, 55]. Especially it is inclined to accumulate residual stresses for crisscross beam structure of porous scaffolds during SLM process. Stress relief annealing (600 °C+FC) can eliminate the residual internal stress of SLM-produced porous samples, so as to prevent the premature deformation and fractures caused by stress concentration. Therefore the samples presented a higher ultimate strength after stress relief annealing. Moreover, as a classical α+β titanium alloy, the Ti-6Al-4V parts can get strengthened and toughened effectively through heat treatment optimizing microstructure. The microstructure of SLM-produced part mainly consists of most acicular metastable α' martensitic and few β phases. After full annealing at a temperature between recrystallization of 750 ℃ and β transition of 995 °C, the uneven martensitic structure transformed to stable coarsened microstructure of (α+β) phase, and avoided the formation of Widmanstatten structure[56]. Consequently, this microstructure transformation reduced the strength but increased the ductility of the scaffolds.

4.3. In vitro cell behavior analysis

The current *in vitro* culture experimental results demonstrated that the SLM-fabricated irregular Ti-6Al-4V scaffolds based on Voronoi-Tessellation had favorable cytocompatibility for orthopedic applications. The inherent characteristics brought by the design and fabrication, including pore characteristic, surface property and mass transport ability, had noteworthy influence on cell attachment, proliferation and differentiation on different scaffolds[5, 16].

The difference in cell amount of scaffolds on day 1 was attributed to the local permeability, which would affect the cells seeding efficiency. According to the Kozeny-Carman equation, the permeability of porous medium was associated with specific surface area and porosity[57]. Smaller pore had a lower permeability, and the scaffold with a higher porosity had a higher permeability. A higher permeability suggested that the cell suspension had less resistance when permeating the scaffold, giving the cells less time to attach to the surface[16, 58]. The set 1 of scaffolds with different irregularities had different pore size distributions (Fig. 5), although having approximate porosity and specific surface area on the whole. The scaffold with irregularity of 0.25 and 0.5 had more smaller pores (＜600 μm), where could be seeded more cells owing to a lower local permeability (Fig. 7(c)). Similarly, under the same design condition, the set 2 of scaffold with porosity of 48.83% had the lowest permeability, resulting in the highest seeding efficiency (Fig. 7(d)). However, the permeability also characterized the mass transport ability of porous scaffold[59], which would affect cell proliferation. The scaffolds with bigger pores or higher porosity would be more suitable for cell sustaining viability and proliferation owning to its greater transport ability for nutrient and oxygen and avoiding pore occlusion. Thus, with the increase in culture time, there were more cells on the scaffold with higher porosity on day 5 (Fig. 7(d)). Particularly, the scaffolds with irregularity of 0.25 and 0.5 had wider pore size distribution (0-1800 μm). Therefore, as the previously reported[16], this combination of small pores and large pores could not only obtain satisfactory cells seeding efficiency in early period, but also guarantee good cell proliferation with the development of the culture process (Fig. 7(c)).

From SEM visualization for the cells seeded on the scaffolds, it was concluded that the SLM-produced Ti-6Al-4V scaffolds were conducive for cell adhesion and spreading. The original rough surface consisted of micro scale pores and ravines, formed by successive melt layers, incompletely melting and welding particles, which could support cells attachment, migration, and proliferation at early time via the provided physical holds. Meanwhile, similar to previous literature reported, human osteoblasts might only bridge irregularly shaped pores smaller than 200 μm[60]. The cell bridging behaviors occurred in the micro scale pores or ravines of struts in early time could be attributed to the following two points. Firstly, during cell seeding step, the surface tension could lock the cell suspension in these small gaps, leading to more cells attaching easily. Secondly, during early culture, the curvature-driven growth effects discovered by Rumpler et al.[61] would make cells prefer to fill the locations with higher curvature, like the micro scale pores and ravines of struts or

the smaller pores (< 200 μm) of scaffolds.

As an early marker of osteoblast differentiation, ALP activity is measured commonly[62]. The present results on day 14 of *in vitro* culture clearly showed SLM-produced Ti-6Al-4V scaffolds had the potential of promoting MG63 cells toward osteoblast differentiation effectively. It has been previously reported that the micrometer-scale roughness of surfaces of Ti-6Al-4V implants could promote osteoblast differentiation[63]. In addition, the scaffolds with irregular porous structure and relatively high porosity were more conducive to enhancing osteoblast differentiation in early period of culture. This was because that the scaffolds with the full irregularity of 0.5 had random porous architecture consisting of pores with a relatively wide size distribution and varied shapes. As with gradient regular porous structure[51, 64], under the premise of providing sufficient nutrients and oxygen, it would make cells exposed to more diversified mechanical stimuli, enhancing osteoblast differentiation. This result was also in accordance with the viewpoints of Lv et al.[65] and Cheng at al.[19], which pointed that the irregular pores of trabecular-like scaffolds could contribute differently to the local growth factor production (such as bone morphogenetic protein-2 and vascular endothelial growth factor) and promote bone formation and ingrowth. However, the trabecular-like porous structure might perform better in inducing osteocyte differentiation due to its biomimetic feature than gradient regular porous structure. On the other hand, cells on scaffolds with higher porosities (63.51% and 74.28%) showed better osteoblast differentiation. It was believed that the increased porosity increased the specific surface area, thus providing more space for cell interaction *in vitro* and promoting osteoblast differentiation. But this result was not in agreement with the common viewpoint that regular scaffolds with lower porosity could stimulate osteogenesis by suppressing cell proliferation and forcing cell aggregation *in vitro*[15]. In fact, osteoblast differentiation is accompanied by cell proliferation[66]. So higher porosity might be beneficial for both. Moreover, it is possible that the irregular structure based on Voronoi-Tessellation gives extra impact on preexisting conditions of osteoblast differentiation. Of course, this idea needs further investigation *in vitro* and *in vivo*.

5. Conclusions

In this study, the irregular porous Ti-6Al-4V scaffolds with different irregularities and porosities were constructed by the Voronoi-Tessellation based method and fabricated by selective laser melting process. The approach based on Voronoi-Tessellation principle and controlled random

points could structurally mimic trabecular bone structure effectively. As a typical AM technique, SLM process exhibited great ability in preparing irregular porous scaffolds. However, it also brought scaffolds some inherent discrepancies with respect to the designed model. The porosity and the irregularity had a significant influence on the mechanical performance of scaffolds. Taking irregularity into consideration, the Gibson-Ashby model no longer applied to the porous structure. Besides, the heat treatment of full annealing could effectively increase the ductility of SLM-produced Ti-6Al-4V porous scaffold but not decrease its strength seriously. Nevertheless, the as-built Ti-6Al-4V scaffolds with porosities of 48.83-74.28% presented a satisfying mechanical performance, which was in the same stiffness level with cancellous bone but had a more excellent stress resistance ability similar to cortical bone. Moreover, primary examination *in vitro* showed that the as-built Ti-6Al-4V scaffolds had a favorable cytocompatibility. The original surface of SLM-fabricated scaffolds was in favor of cell adhesion and migration, because of micro scale pores and ravines. The trabecular-like porous scaffolds with the full irregularity (0.5) and higher porosity (63.51%, 74.28%) did better at enhancing osteoblast proliferation and differentiation because of the preferable combination of small and large pores with varied shapes.

In conclusion, the present study revealed that the SLM-fabricated trabecular-like Ti-6Al-4V scaffold based on Voronoi-Tessellation had the possibility for orthopedic application due to its controllable mechanical properties and potential advantage of enhancing osteoblast differentiation. Our future work will focus on the investigation for *in vivo* biocompatibility of this scaffold.

Acknowledgments

The work was financially supported by the Advanced Research Project of Army Equipment Development (No. 301020803), the Key Research and Development Program of Jiangsu (No. BE 2015161), the Young Scientists Fund of the National Natural Science Foundation of China (No. 51605473), the Jiangsu Provincial Research Foundation for Basic Research, China (No. BK 20161476), the Science and Technology Planning Project of Jiangsu Province of China (No. BE 2015029) and the Science and Technology Support Program of Jiangsu (Nos. BE 2014009-1, BE 2014009-2 and BE 2016010-3).

References

[1] M. Schieker, W. Mutschler, Der Unfallchirurg 109 (2006) 715-732.

[2] H.M. Frost, Angle Orthod. 74 (2004) 3-15.

[3] S.J. Hollister, Adv. Mater. 21 (2009) 3330-3342.

[4] M.J. Olszta, X. Cheng, S.S. Jee, R. Kumar, Y.Y. Kim, M.J. Kaufman, E.P. Douglas, L.B. Gower, Mater. Sci. Eng. R 58 (2007) 77-116.

[5] L.L. Hench, J. Am. Ceram. Soc. 74 (1991) 1487-1510.

[6] X.H. Liu, P.X. Ma, Ann. Biomed. Eng. 32 (2004) 477-486.

[7] K. Alvarez, H. Nakajima, Materials (Basel) 2 (2009) 790-832.

[8] Y. Yang, F. Yuan, C. Gao, P. Feng, L. Xue, S. He, C. Shuai, J. Mech. Behav. Biomed. Mater. 82 (2018) 51-60.

[9] Y. Yang, X. Guo, C. He, C. Gao, C. Shuai, ACS Biomater. Sci. Eng. 4 (2018) 1046-1054.

[10] Y. Yang, P. Wu, Q. Wang, H. Wu, Y. Liu, Y. Deng, Y. Zhou, C. Shuai, Materials 9 (2016) 1-10.

[11] M. Textor, C. Sittig, V. Frauchiger, S. Tosatti, D.M. Brunrtte, In: D. M. Brunrtte, P. Tengvall, M. Textor, P. Thomsen (Eds.), Titanium in Medicine, Springer, Berlin, 2001, pp. 171-230.

[12] W. Xue, B.V. Krishna, A. Bandyopadhyay, S. Bose, Acta Biomater. 3 (2007) 1007-1018.

[13] S.M. Giannitelli, D. Accoto, M. Trombetta, A. Rainer, Acta Biomater. 10 (2014) 580-594.

[14] X. Wang, S. Xu, S. Zhou, W. Xu, M. Leary, P. Choong, M. Qian, M. Brandt, Y.M. Xie, Biomaterials 83 (2016) 127-141.

[15] V. Karageorgiou, D. Kaplan, Biomaterials 26 (2005) 5474-5491.

[16] B.S. Van, Y.C. Chai, S. Truscello, M. Moesen, G. Kerckhofs, O.H. Van, J.P. Kruth, J. Schrootrn, Acta Biomater. 8 (2012) 2824-2834.

[17] Z. Wang, C. Wang, C. Li, Y. Qin, L. Zhong, B. Chen, Z. Li, H. Liu, F. Chang, J. Alloys Compd. 717 (2017) 271-285.

[18] D.K. Pattanayak, A. Fukuda, T. Matsushita, M. Takemoto, S. Fujibayashi, K. Sasaki, N. Nishida, T. Nakamura, T. Kokubo, Acta Biomater. 7 (2011) 1398-1405.

[19] A. Cheng, A. Humayun, D.J. Cohen, B.D. Boyan, Z. Schwartz, Biofabrication 6 (2014) 045007.

[20] M.L. Mather, S.P. Morgan, L.J. White, H. Tai, W. Kockenberger, S.M. Howdle, K.M. Shakesheff, J.A. Crowe, Biomed. Mater. 3 (2008) 015011.

[21] Z. Chen, Z. Su, S. Ma, X. Wu, Z. Luo, Comput. Meth. Prog. Biomed. 88 (2007) 123-130.

[22] X.Y. Kou, S.T. Tan, Comput. Aided Des. 42 (2010) 930-941.

[23] S. Nachtrab, S.C. Kapfer, C.H. Arns, M. Madadi, K. Mecke, G.E. Schröder-Turk, Adv. Mater.

23 (2011) 2633-2637.

[24] X. Zhang, L. Tang, Z. Liu, Z. Jiang, Y. Liu, Y. Wu, Mech. Mater. 104 (2017) 73-84.

[25] L. Lin, X. Wang, X. Zeng, CMES Comput. Model. Eng. Sci. 98 (2014) 203-220.

[26] H. Honda, T. Nagai, J. Biochem. 157 (2015) 129-136.

[27] M. Fantini, M. Curto, C.F. De, Virtual. Phys. Prototyp. 11 (2016) 77-90.

[28] S. Gómez, M.D. Vlad, J. López, E. Fernández, Acta Biomater. 42 (2016) 341-350.

[29] K.F. Leong, C.M. Cheah, C.K. Chua, Biomaterials 24 (2003) 2363-2378.

[30] J.P. Kruth, G. Levy, F. Klocke, T.H.C Childs, CIRP. Ann. Manuf. Technol. 56 (2007) 730-759.

[31] L. Thijs, F. Verhaeghe, T. Craeghs, J.V. Humbeeck, J.P. Kruth, Acta Mater. 58 (2010) 3303-3312.

[32] P.H. Warnke, T. Douglas, P. Wollny, E. Sherry, M. Steiner, S. Galonska, S.T. Becker, I.N. Springer, J. Wiltfang, S. Sivananthan, Tissue Eng. Part. C 15 (2009) 115-124.

[33] G. Wang, L. Shen, J. Zhao, H. Liang, D. Xie, Z. Tian, C. Wang, ACS Biomater. Sci. Eng. 4 (2018) 719-727.

[34] B. Vandenbroucke, J.P. Kruth, Rapid. Prototyp. J. 13 (2007) 196-203.

[35] S. Langlois, F. Coeure, I. Material. Characterization. J. Appl. Electrochem. 19 (1989) 43-50.

[36] I. Mircheski, M. Gradišar, Comput. Methods Biomech. Biomed. Eng. 19 (2016) 1531-1540.

[37] Z. Xiao, Y. Yang, R. Xiao, Y. Bai, C. Song, D. Wang, Mater. Des. 143 (2018) 27-37.

[38] C. Yan, L. Hao, A. Hussein, D. Raymont, Int. J. Mach. Tools Manuf. 62 (2012) 32-38.

[39] S. McKown, Y. Shen, W.K. Brookes, C.J. Sutcliffe, W.J. Cantwell, G.S. Langdon, G.N. Nurick, M.D. Theobald, Int. J. Impact. Eng. 35 (2008) 795-810.

[40] L.J. Gibson, M.F. Ashby. Cellular Solids: Structure and Properties, second ed., Cambridge University Press, Cambridge, 1999, pp. 175-231.

[41] Y.Z. Yang, J.M. Tian, J.T. Tian, Z.Q. Chen, X.J. Deng, D.H. Zhang, J. Biomed. Mater. Res. 52 (2000) 333-337.

[42] D.A. Hollander, W.M. Von, T. Wirtz, R. Sellei, B. Schmidt-Rohlfing, O. Paar, H.J. Erli, Biomaterials 27 (2006) 955-963.

[43] M. Fantini, M. Curto, Int. J. Interact. Des. Manuf. 12 (2018) 585-596.

[44] S.L. Sing, F.E. Wiria, W.Y. Yeong, Robot. Comput. Integr. Manuf. 49 (2018) 170-180.

[45] L. Mullen, R.C. Stamp, W.K. Brooks, E. Jones, C.J. Sutcliffe, J. Biomed. Mater. Res. Part B

89 (2009) 325-334.

[46] P. Sevilla, C. Aparicio, J.A. Planell, F.J. Gil, J. Alloys Compd. 439 (2007) 67-73.

[47] E.F. Morgan, H.H. Bayraktar, T.M. Keaveny, J. Biomech. 36 (2003) 897-904.

[48] X.N. Gu, Y.F. Zheng, Front. Mater. Sci. China 4 (2010) 111-115.

[49] J. Shi, J. Yang, Z. Li, L. Zhu, L. Li, X. Wang, J. Alloys Compd. 728 (2017) 1043-1048.

[50] L. Zhu, L. Li, J. Shi, Z. Li, J. Yang, Am. J. Transl. Res. 10 (2018) 3443-3454.

[51] E. Onal, J.E. Frith, M. Jurg, X. Wu, A. Molotnikov, Metals 8 (2018) 1-21.

[52] J. Parthasarathy, B. Starly, S. Raman, A. Christensen, J. Mech. Behav. Biomed. Mater. 3 (2010) 249-259.

[53] R.W. McCalden, J.A. McGlough, M.B. Barker, C.M. Court-Brown, J. Bone Joint Surg. Am. 75 (1993) 1193-1205.

[54] P. Mercelis, J.P. Kruth, Rapid. Prototyp. J. 12 (2006) 254-265.

[55] T. Vilaro, C. Colin, J.D. Bartout, Metall. Mater. Trans. A 4 (2011) 3190-3199.

[56] B. Vrancken, L. Thijs, J.P. Kruth, H.J. Van, J. Alloys Compd. 54 (2012) 177-185.

[57] A. Costa, Geophys. Res. Lett. 33 (2006) 1-5.

[58] L. Shor, S. Güçeri, X. Wen, M. Gandh, W. Sun, Biomaterials 28 (2007) 5291-5297.

[59] M.R. Dias, P.R. Fernandes, J.M. Guedes, S.J. Hollister, J. Biomech. 45 (2012) 938-944.

[60] W. Xue, B.V. Krishna, A. Bandyopadhyay, S. Bose, Acta Biomater. 3 (2007) 1007-1018.

[61] M. Rumpler, A. Woesz, J.W.C. Dunlop, D.J.T. Van, P. Fratzl, J. Royal Soc. Interf. 5 (2008) 1173-1180.

[62] E.G. Khaled, M. Saleh, S. Hindocha, M. Griffin, W.S. Khan, Open. Orthop. J. 5 (2011) 289-295.

[63] Z. Schwartz, P. Raz, G. Zhao, Y. Barak, M. Tauber, H. Yao, B.D. Boyan, J. Bone Joint Surg. Am. 90 (2008) 2485-2498.

[64] K.C. Nune, A. Kumar, R.D.K. Misra, S.J. Li, Y.L. Hao, R. Yang, Colloid. Surf. B 150 (2017) 78-88.

[65] J. Lv, Z. Jia, J. Li, Y. Wang, J. Yang, P. Xiu, K. Zhang, H. Cai, Z. Liu, Adv. Eng. Mater. 17 (2015) 1391-1398.

[66] S.J. Roberts, Y. Chen, M. Moesen, J. Schrooten, F.P. Luyten, Stem Cell Res. 7 (2011) 137-144.

Figure list：

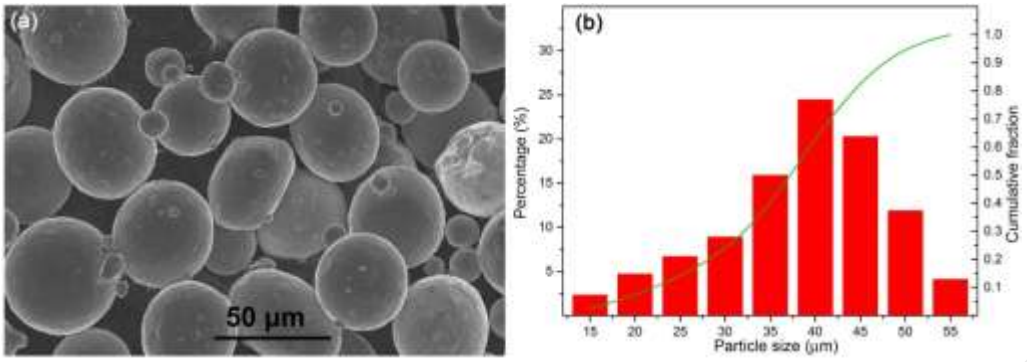

Fig. 1. (a) SEM micrograph and (b) particle size distribution of Ti-6Al-4V powders.

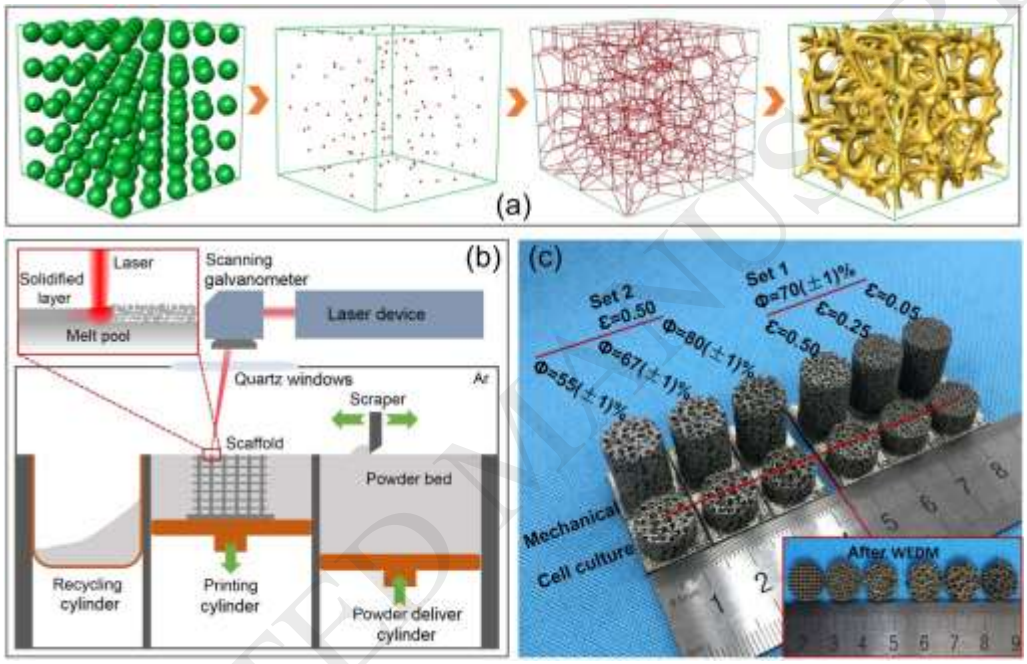

Fig. 2. (a) Schematic of irregularly porous structure modeling, (b) schematic of selective laser melting process and (c) as-built Ti-6Al-4V scaffolds by SLM.

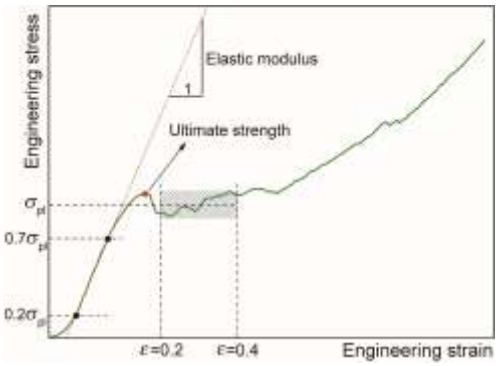

Fig. 3. Stress-strain curve to determine characteristic values from compression testing of porous structure.

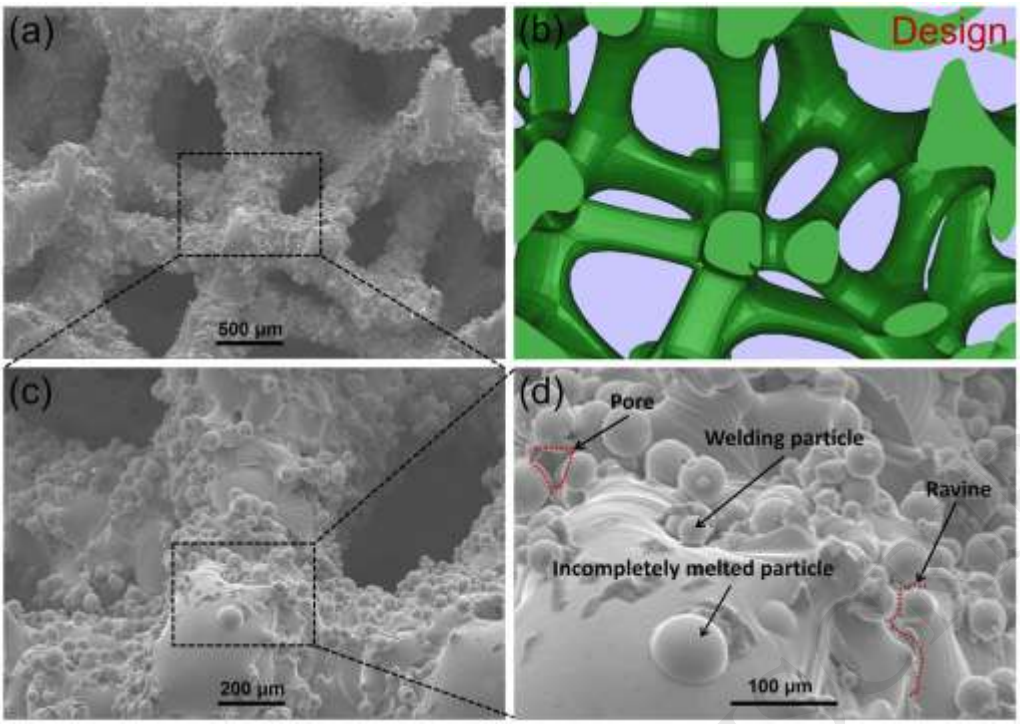

Fig. 4. (a, c, d) SEM micrographs with different amplifications of as-built Ti-6Al-4V scaffolds after ultrasonic cleaning and (b) 3D model.

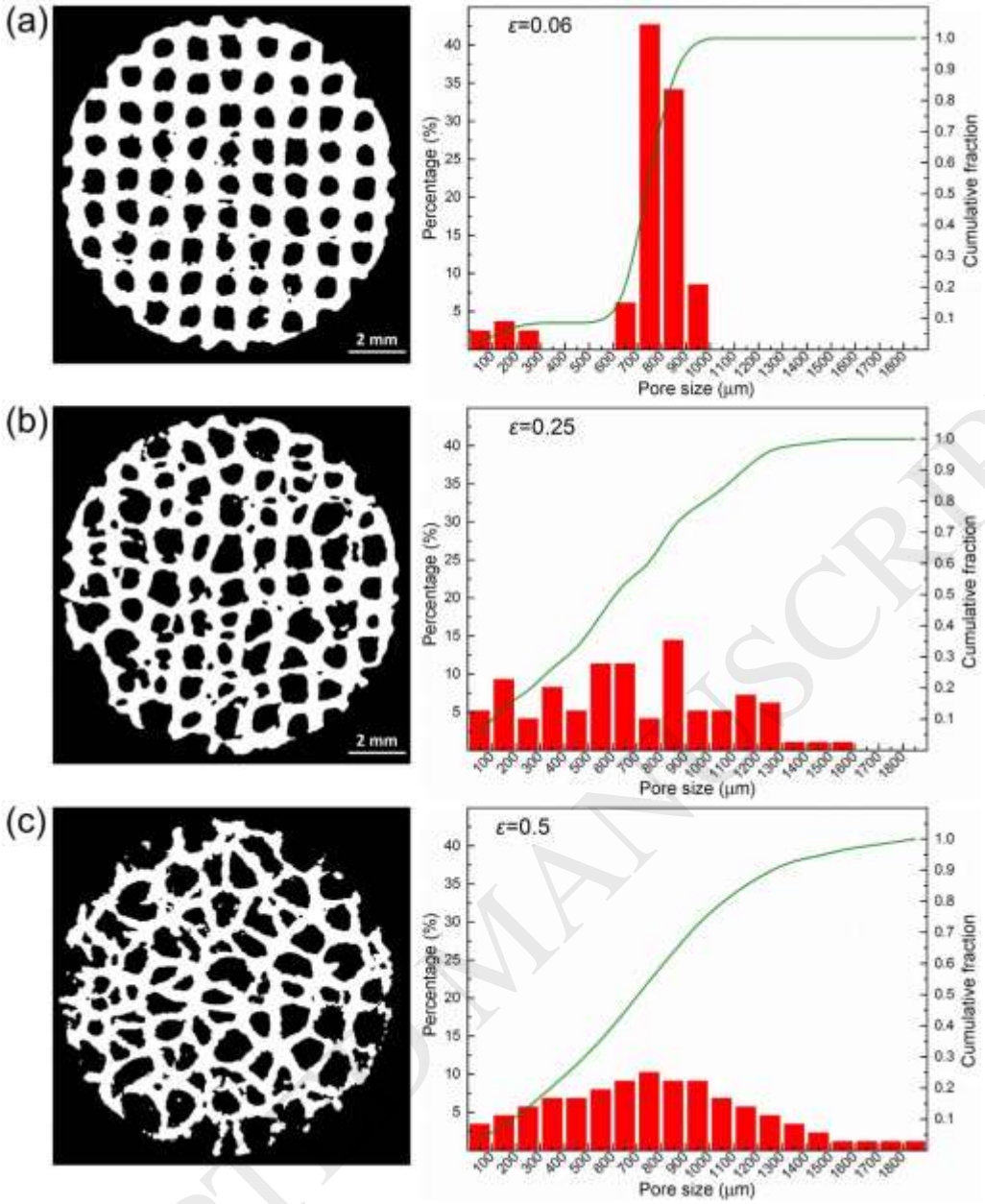

Fig. 5. Relationship between pore size distribution and irregularity for set 1 of as-built scaffolds: (a) ε=0.06; (b) ε=0.25; (c) ε=0.5.

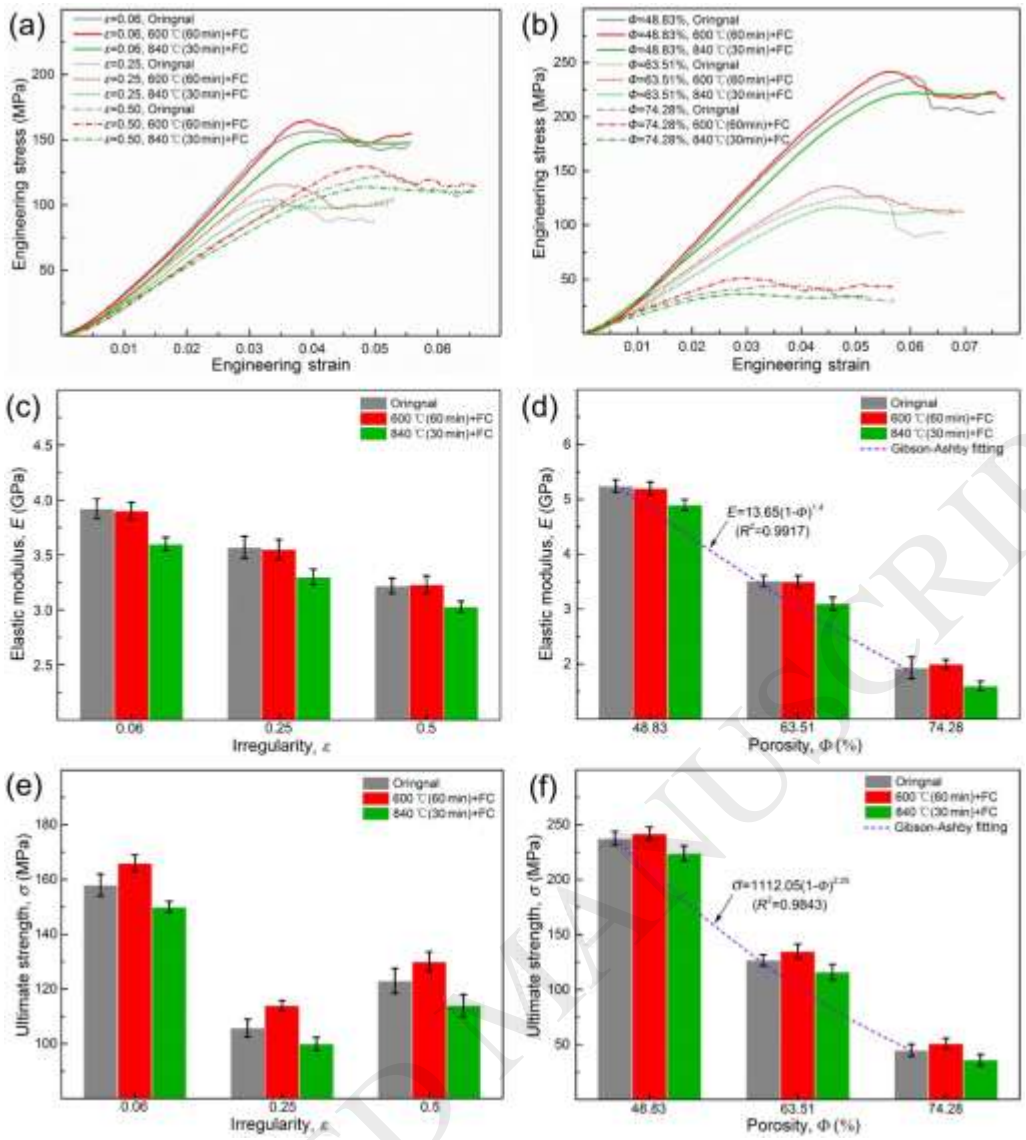

Fig. 6. Compression test results of as-built scaffolds with various irregularities, porosities and different heat treatment processes: (a, b) stress-strain curves; (c, d) calculated elastic modulus; (e, f) ultimate strength.

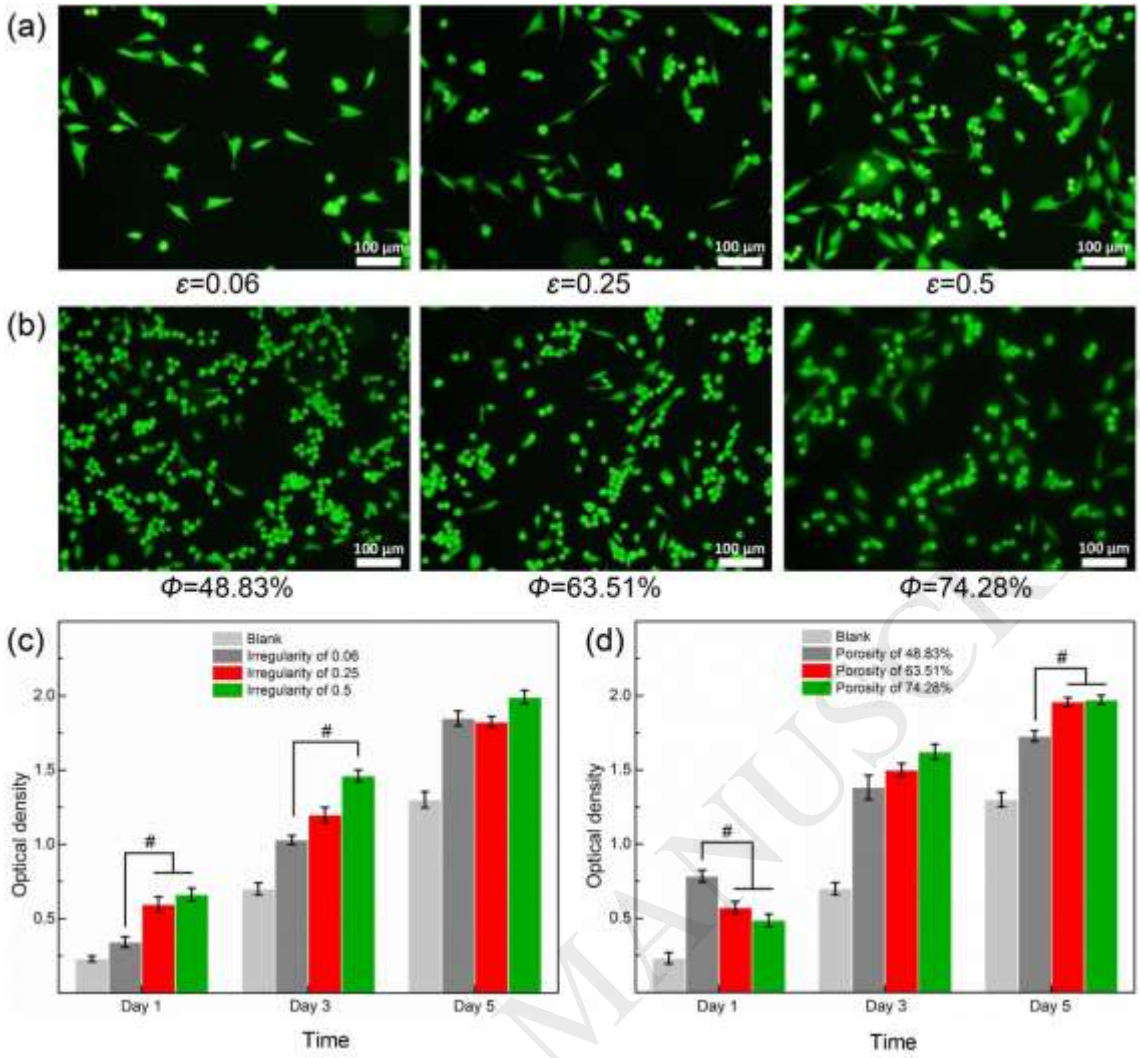

Fig. 7. Viability and proliferation of MG63 cells on porous Ti-6Al-4V scaffolds with different irregularities and porosities: (a, b) fluorescence microscopy images after being cultured for 1 d (live cells appeared as bright green dots); (c, d) CCK-8 assay results after being cultured for 1, 3 and 5 d, n=3 (sample size), $^{\#}$Ssamlignificant difference (one-way ANOVA: $p<0.05$).

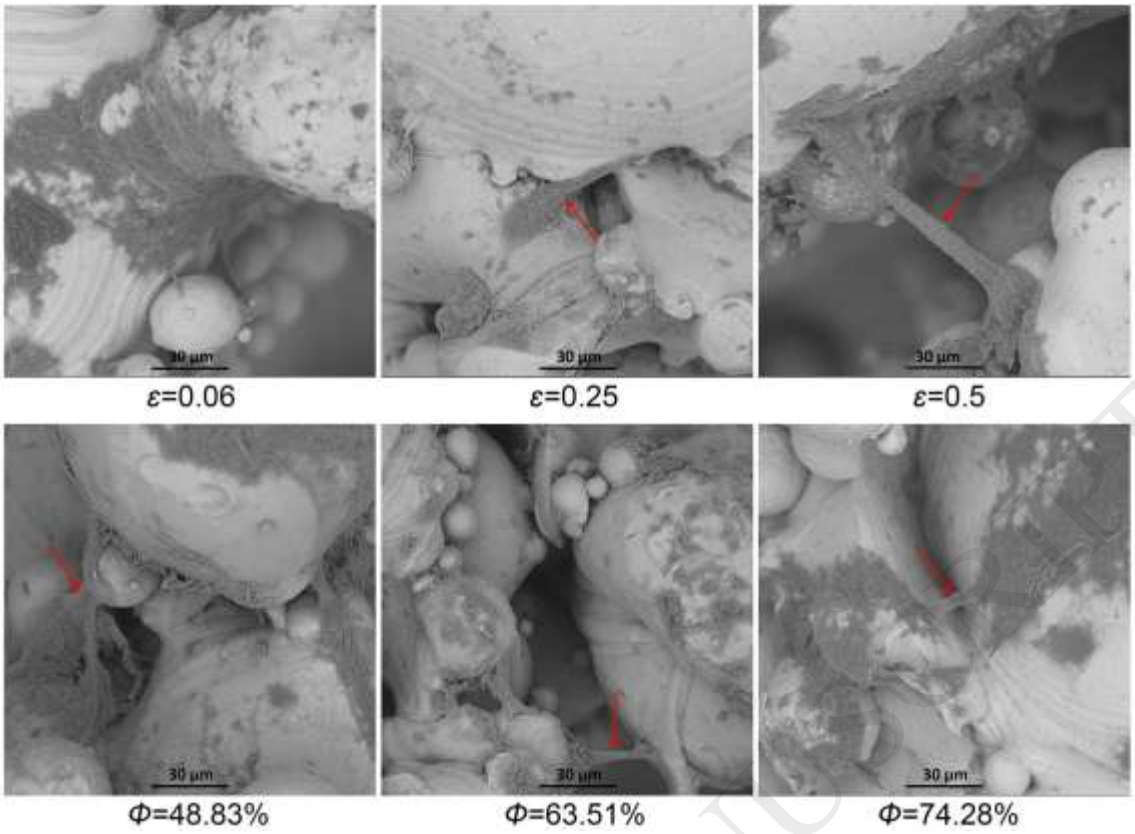

Fig. 8. SEM micrographs of cell adhesion morphologies on scaffolds with different irregularities and porosities after being cultured for 3 d (cell bridging behaviors were highlighted by red arrows).

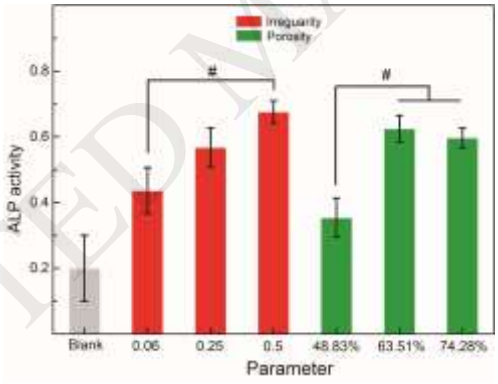

Fig. 9. ALP activity of MG63 cells on different porous Ti-6Al-4V scaffold designs after being cultured for 14 d, n=3 (sample size), $^{\#}$Ssamlignificant difference (one-way ANOVA: $p<0.05$).

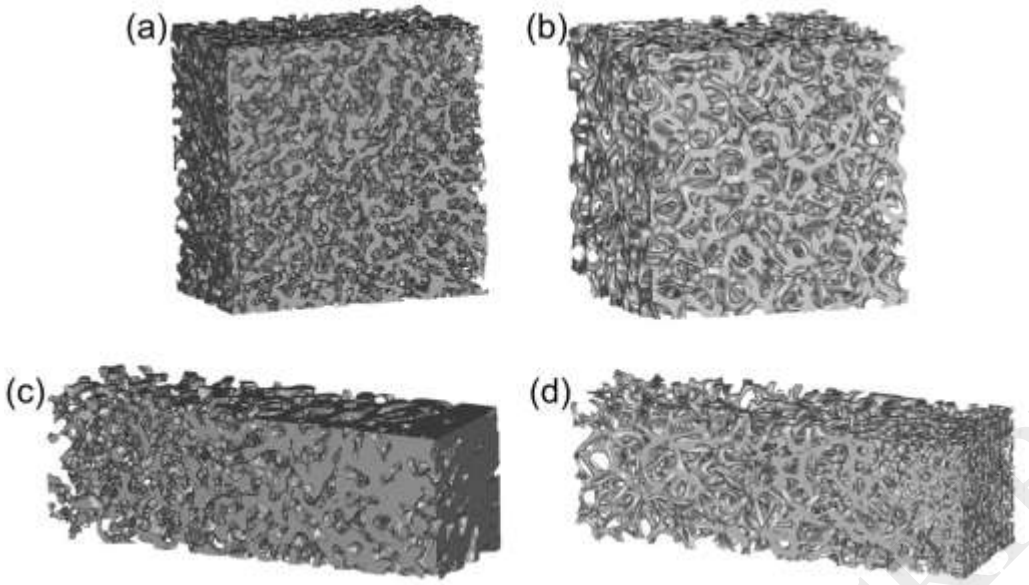

Fig. 10. (a) Reconstructed 3D model of healthy spongy bone with, (b) trabecular-like porous structure with homogeneity in porosity, (c) reconstructed 3D model of gradient structure of trabecular bone and (d) trabecular-like porous structure with gradient in porosity.

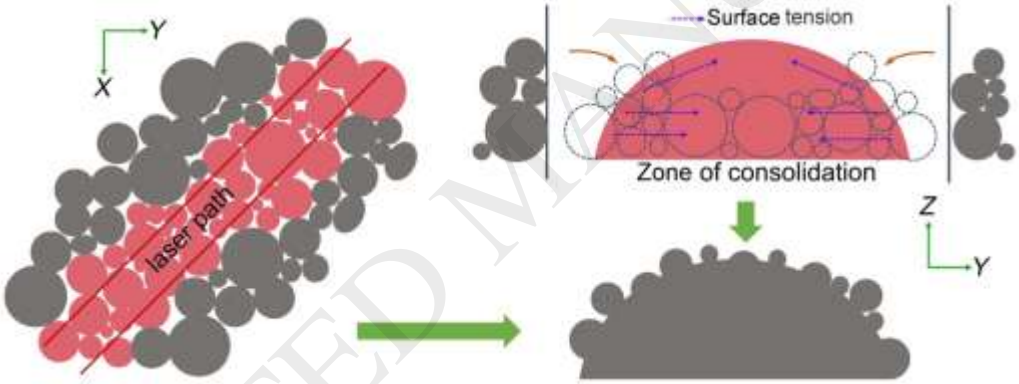

Fig. 11. Forming mechanism of powder adhesions on struts.

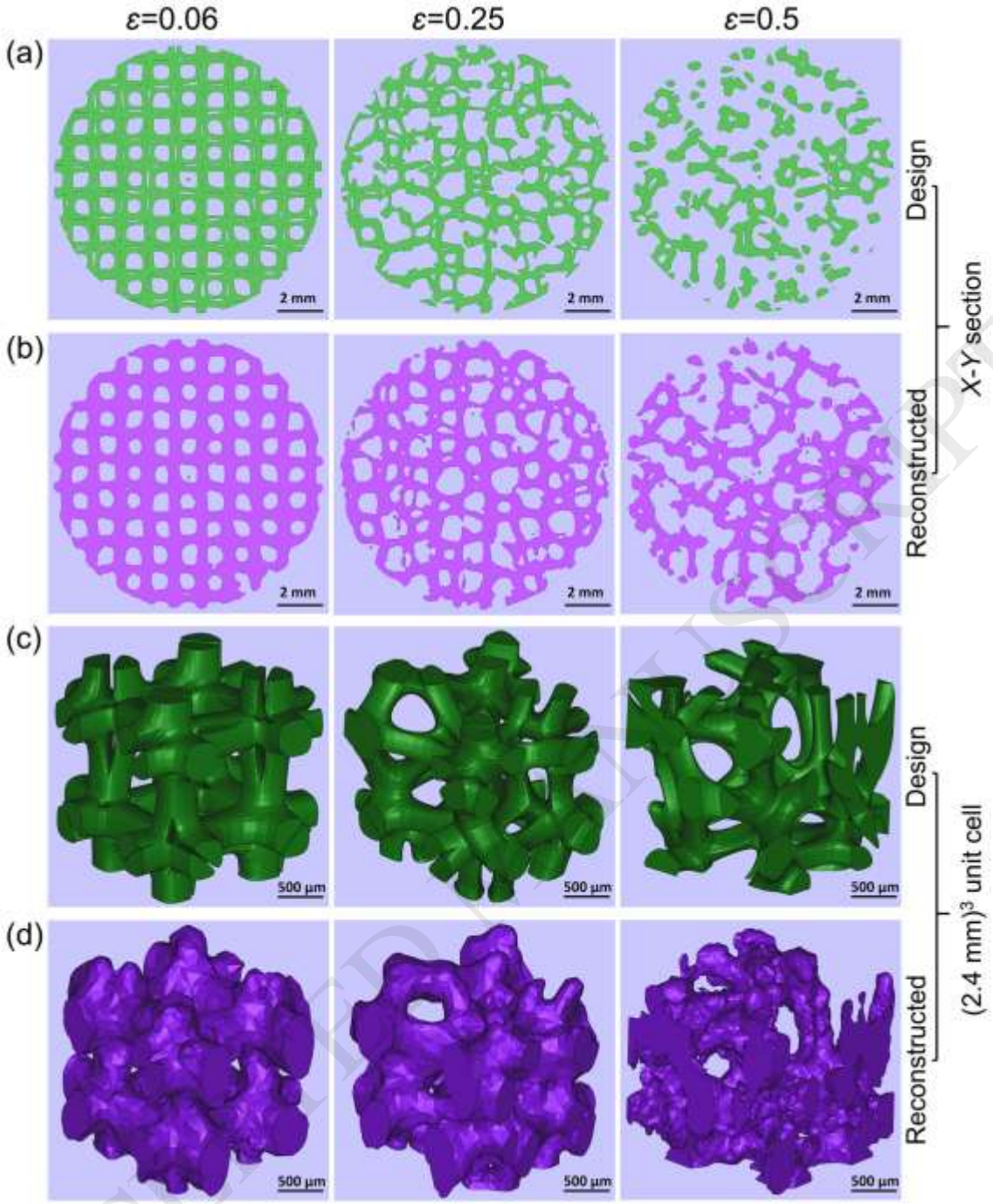

Fig. 12. Comparisons between design and fabrication of scaffolds with different irregularities: (a, b) sections from the same location; (b) unit cells of 2.4 mm × 2.4 mm × 2.4 mm.

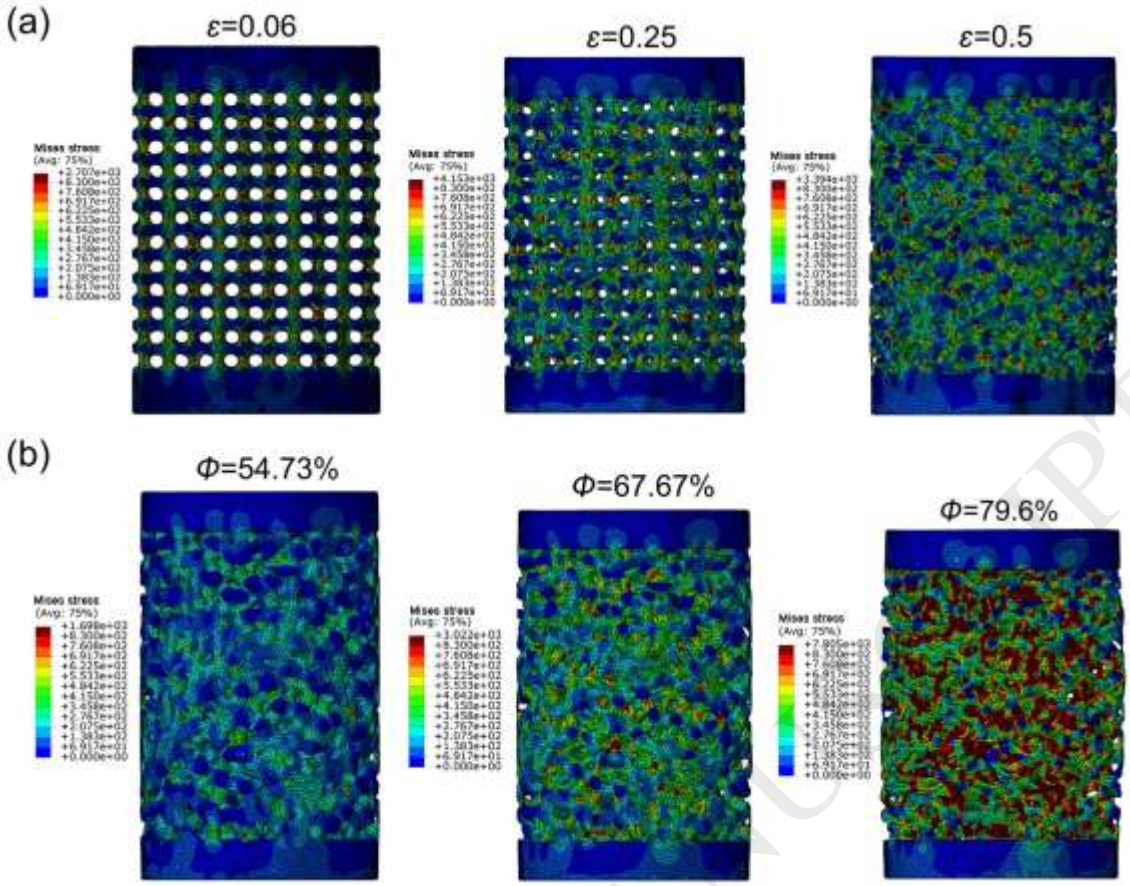

Fig. 13. FEA results for von Mises stress field of scaffolds.

Table list：

Table 1 Chemical composition of the Ti-6Al-4V ELI powder (mass %).

Ti	Al	V	O	N	C	H	Fe
Bal	5.90	3.91	0.12	0.05	0.08	0.012	0.3

Table 2 Optimized process parameters used in the SLM fabrication.

Laser power	Scan speed	Hatch spacing	Layer thickness	Laser focus	Atmosphere
180 W	1350 mm/s	0.1 mm	0.03 mm	0.1 mm	Ar

Table 3 Comparison between the designed and experimental characteristics of scaffolds (n=3; D: difference value).

	ε	Strut thickness (μm)		Volume (mm^3)		Surface area (mm^2)		Specific surface area (mm^{-1})			Porosity (%)		
		CAD	μCT	CAD	μCT	CAD	μCT	CAD	μCT	D	CAD	μCT	D
Set 1	0.06	361±35	611±52	85.49	113.23	890.32	794.75	10.41	7.01	-3.4	70.92	61.49	-9.43
	0.25	352±62	487±49	87.93	109.81	884.33	830.24	10.06	7.56	-2.5	70.01	62.65	-7.36
	0.5	368±81	464±41	89.67	106.67	929.53	895.92	10.37	8.4	-1.97	69.5	63.95	-5.55
Set 2	0.5	730±56	797±34	133.08	150.44	789.53	756.71	5.93	5.03	-0.9	54.73	48.83	-5.9
		550±61	630±21	95.04	107.29	709.16	673.54	7.46	6.28	-1.18	67.67	63.51	-4.16
		380±49	468±39	59.98	75.63	588.31	547.28	9.81	7.23	-2.58	79.6	74.28	-5.32